Thin-Walled Structures 131 (2018) 547–555

Contents lists available at ScienceDirect

Thin-Walled Structures

journal homepage: www.elsevier.com/locate/tws

Full length article

# Crushing behavior and energy absorption performance of a bio-inspired metallic structure: Experimental and numerical study

Alper Tasdemirci*, Emine Fulya Akbulut, Erkan Guzel, Firat Tuzgel, Atacan Yucesoy, Selim Sahin, Mustafa Guden

*Dynamic Testing and Modeling Laboratory and Department of Mechanical Engineering, Izmir Institute of Technology, Gülbahçe Köyü, Urla, Izmir 35430, Turkey*

ARTICLE INFO

*Keywords:*
Biomimicry
Bio-inspired structures
Crushing behavior
Energy absorption
Micro inertia
LSDYNA

ABSTRACT

A thin-walled structure inspired from a biologic creature known as balanus was investigated experimentally and numerically under quasi-static and dynamic loads for load-carrying and energy absorption properties. The structure was composed of an inner conical core with a hemispherical cap and an outer shell in frusto-conical shape and formed by deep drawing. The applied deep drawing process was modelled using nonlinear finite element code LS-DYNA to determine the residual stress/strain and the non-linear thickness distribution after the forming process. It was also shown that the load carried by the balanus structure was greater than the arithmetic sum of the load carried by the inner core and by the outer shell separately. Although the mean force increase due to interaction effect at quasi-static strain rate was approximately 5%, while it increased to roughly 26% at dynamic strain rates in drop weight experiments. The numerical models also showed that the outer shell absorbed more energy than the inner core while the difference between the energy absorbing performance of the core and shell decreased with increasing deformation rate. The effect of strain rate and inertia on the increase in crush load increased with increasing impact velocity, while the strain rate effect had greater influence than the inertia on the crush load. The increased load carrying capacity of the balanus at quasi-static and dynamic strain rates was ascribed to the interaction between the core and shell and the confinement effect of the outer shell particularly at dynamic strain rate.

## 1. Introduction

One of the earliest studies on the axial crushing of thin-walled cylindrical tubes dates back to 1960s [1]. A relationship between the crush force and shell thickness of metallic thin-walled tubes was derived. A self-consistent theory of the progressive folding of thin-walled rectangular columns showed that two-thirds of the plastic energy was dissipated through in-extensional deformations at stationary and moving plastic hinge lines [2]. Experimental studies performed on the tapered thin-walled rectangular cross-section metallic tubes [3,4] showed that the initial peak load decreased with increasing taper sides and the crush force efficiency increased with increasing the number of oblique sides. It was also found that the energy absorption response of tapered tubes could be controlled via their wall thickness and taper angle [5]. The crushing behavior of conical structures were also investigated [6–9]. Results have shown that thin-walled conical frusta deform under axial loading in three different modes: inversion, concertina and diamond. The most substantial variables on the energy absorbing performance were the angle and thickness rather than the bottom diameter and length of the structure [9]. In a combined geometry of a conical portion and a hemispherical cap, the hemispherical cap initially deformed by flattening followed by inward dimpling, while the conical part deformed by progressive axisymmetric folding [10]. The energy absorption of hemispherical cap was found higher under dynamic loading than quasi-static loading, attributed to the strain rate sensitivity of cap material and inertial effects [11].

When thin-walled single metallic tubes are filled with a light-weight foam, an interaction effect exists between tube wall and foam filler [12–17]. Mainly due to this interaction, the crushing forces of foam-filled tubes are higher than the sum of the crushing forces of foam (alone) and tube (alone). The encroachment of the metal tube wall into foam filler was proposed to be resulting in an additional compression in the foam filler, retarding the sectional collapse of the column [14]. The foam filling was also shown to increase the number of folds formed and decrease the fold lengths in the metallic tubes [18]. Further, the tendency for the concertina mode of deformation increased with foam filling due to the thickening effect of foam filling. Recent studies have been also on the single, double, multi-wall and multi-cell tubes [19,20].

* Corresponding author.
*E-mail address:* alpertasdemirci@iyte.edu.tr (A. Tasdemirci).

https://doi.org/10.1016/j.tws.2018.07.051
Received 22 November 2017; Received in revised form 22 July 2018; Accepted 30 July 2018
Available online 03 August 2018
0263-8231/ 

(a)

(b)

**Fig. 1.** (a) Balanus [35] and (b) bio-inspired geometry.

It has been noted that the similar interaction effect existed between the outer and inner tubes of bitubular structures [21] and concentric expanded metal tubes under quasi-static axial compression [22,23].

The geometry of balanus, a sea creature found on coastlines along the oceans, is composed of a conical inner core and an outer shell (Fig. 1(a)), resembling bitubular tubes. The balanus exist in extreme conditions such as on the rocks and man-made structures from mid-shore to the neritic zone and also forms part of the fouling community on the hulls of ships. The geometry of the balanus should therefore be optimized to the externally applied natural forces. As with the other bio-inspired structures such as honeycombs [24], turtle shells [25], beetle forewings [26] and peacock mantis shrimps [27], the geometry of the balanus is interesting for the development of crashworthy structures as it accommodates all three parts together: bitubular and conical form and a hemispherical part. Present study aims to investigate both experimentally and numerically the deformation behavior, load carrying capacity and energy absorption of a thin-walled bio-inspired structure under quasi-static and dynamic loadings. The applications of such structure may include the crash bumpers of vehicles to absorb the crush energy during a collision and also the core material of sandwiches for the structural protection against blast loading.

## 2. Materials and testing

The constituents of the bio-inspired structure were formed by a deep drawing process using an AISI 304L stainless steel blank having 0.5 mm thickness. The deep drawing process was composed of sheet forming and trimming. The sheet forming was accomplished in two stages. The hemispherical cap of the inner core and the flat-top portion of the outer shell were formed in the first stage, while the conical parts of the components having the desired angle, height and diameter were formed in the second stage. The plastic strain in the first stage was below the fracture strain of the blank material and trimming was applied to remove the excess elongations in the skirt and the upper region the outer shell. The top and bottom diameters of the outer shell, the bottom diameter of the core and the height of the both constituents are 15.5, 30, 29 and 24.9 mm, respectively.

The yield strength, elastic modulus and failure strain of AISI 304L stainless steel sheet metal were determined from the tensile tests conducted at quasi-static and high strain rates. The quasi-static tests were performed in a Shimadzu universal test machine in accord with ASTM E8M-04 standard [28]. The axial displacement of the test sample was recorded by a video extensometer. The high strain rate tensile tests were performed in a Split Hopkinson Tension Bar (SHTB). The used SHTB set-up was made of 2 cm-diameter 316 L stainless steel bars, with a striker tube length of 30 cm, incident bar length of 244 cm and transmitter bar length of 244 cm. The elastic modulus, density and yield strength of the bar material are 193 GPa, 8 g $cm^{-3}$ and ~ 300 MPa, respectively. In SHTB test, a gas gun fires a striker tube with an inner diameter of 2 cm and outer diameter of 2.9 cm to the stepped end of the

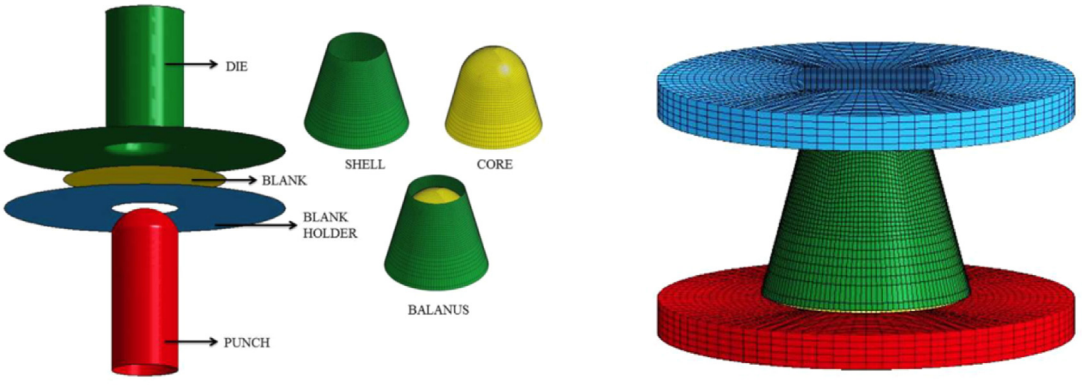


(a) (b)

**Fig. 2.** (a) The model of deep drawing process and (b) compression test model.

**Table 1**
Johnson-Cook model parameters of AISI 304L stainless steel.

| ρ (g cm$^{-3}$) | G (GPa) | E (GPa) | v | A (MPa) | B (MPa) | n | c | $D_1$ | $D_2$ |
|---|---|---|---|---|---|---|---|---|---|
| 7.83 | 80 | 193 | 0.305 | 218 | 1905 | 0.88 | 0.125 | 0.857 | − 0.011 |

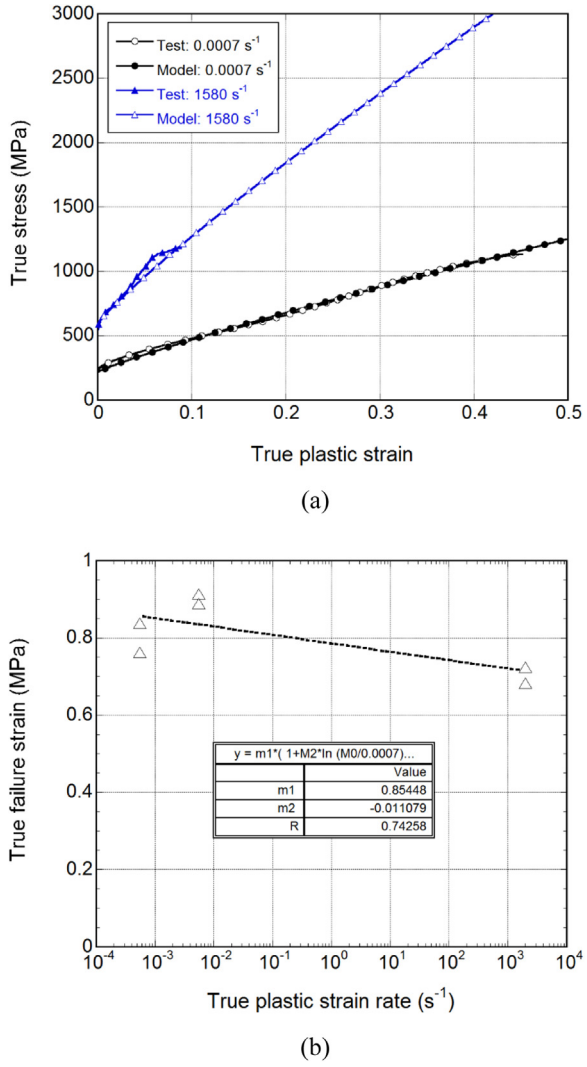


**Fig. 3.** (a) Experimental tensile stress-strain curves of AISI 304L steel at quasi-static and high strain rates and the JC flow stress model fit and (b) failure strain and JC failure strain fit.

incident bar. This creates a tension wave on the incident bar which moves to the sample bar interface where it is partly reflected as compressive wave to the incident bar and partly transmitted as tension wave to the transmitter bar. The incident, reflected and transmitted strains are measured by means of strain gages mounted on the incident and transmitter bars. The SHTB tests were performed on non-standard plate test specimens of 0.5 mm in thickness, 4 mm width and 2 mm in length. The tests were monitored using a Photron Fastcam high-speed camera. The strain rate ($\dot{\varepsilon}$), the strain ($\varepsilon$), and the stress ($\sigma$) of the specimens in SHTB were determined using the following equations based on one-dimensional wave propagation in long bars:

$$\dot{\varepsilon}(t) = \frac{-2C_b}{L_s}\varepsilon_r(t) \tag{1}$$

$$\varepsilon(t) = \frac{-2C_b}{L_s}\int_0^t \varepsilon_r dt \tag{2}$$

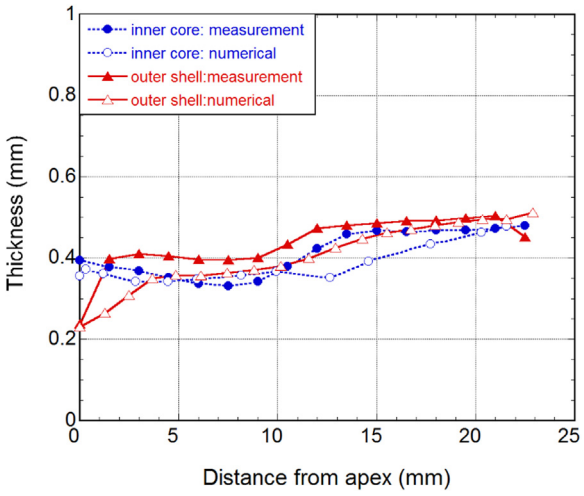


**Fig. 4.** Measurement and experimental thickness distribution of the inner core and the outer shell.

$$\sigma(t) = \frac{E_b A_b \varepsilon_t}{A_s} \tag{3}$$

where $C_b$, $L_s$, $E_b$, $A_b$, $A_s$, $\varepsilon_r$ and $\varepsilon_t$ are sequentially elastic wave speed of the bar, the length of the specimen, the elastic modulus of the bar, the cross-section area of the bar, the cross-section area of the specimen and incident and transmitted strains.

The quasi-static crushing experiments of the bio-inspired structure were performed in the Shimadzu universal test machine with a cross-head speed of 0.025 mm s$^{-1}$. In these tests, the specimens were placed between the compression test plates and the top rigid plate compressed the structure at a constant cross-head speed, while the bottom rigid plate was fully constrained. The dynamic crushing tests were performed in a Fractovis Plus drop weight test machine at an impact velocity of 4 m s$^{-1}$, which was equipped with a flat striker tip of 70 mm. A velocity sensor was used to determine the impact velocity of the striker tip. The deformation histories of impact tests were monitored using the high-speed camera. At least five specimens were tested for each of the samples investigated.

## 3. Modelling

The deep drawing process and crushing experiments were simulated using nonlinear finite element code LS-DYNA 971 [29]. A three-dimensional deep drawing finite element model was used to generate the core structure numerically. All constituents were modelled with Belytschko-Tsay shell element with five integration points through the thickness. The numerical model constituents of the forming process of the inner core are shown in Fig. 2(a). All parts except the blank were assumed rigid. The boundary prescribed motion rigid card was activated to define the speed of the punch. The punch in the model moved along the die cavity to give a shape to the blank which was placed between the blank-holder and die.

The deep-drawn geometries (shell, core and balanus structure) retained substantial amount of residual strain and stress after the deep-drawing process. Numerically, LS-DYNA 971 allows users to perform subsequent simulations such as trimming and forming using the “dynain” file generation method [29,30]. The dynain file was incorporated

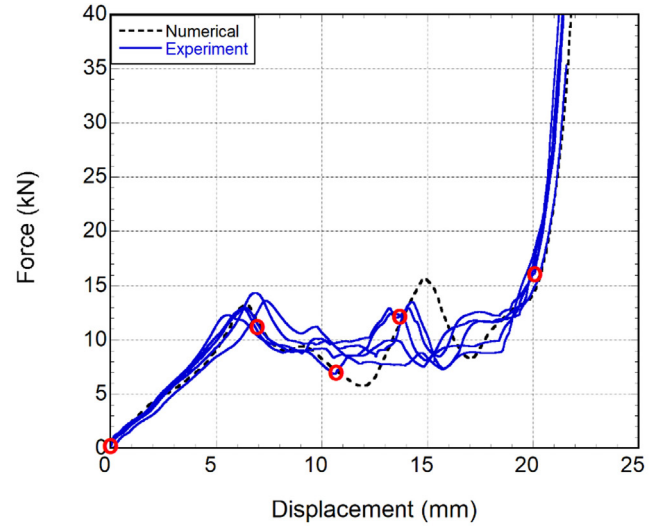


(a)

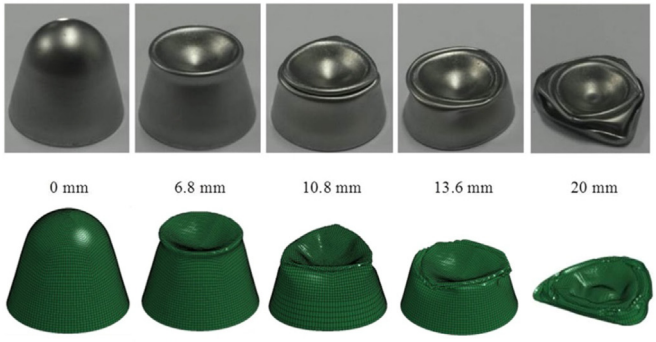


(b)

**Fig. 5.** (a) Experimental (5 tests) and numerical force–displacement curves of the inner core at quasi-static strain rates and (b) the pictures of the deformed specimens.

into a new LS-DYNA 971 input deck for quasi-static and dynamic crushing simulations. The deformation of AISI 304L stainless steel was modelled using the Johnson-Cook (JC) flow stress model and damage model [31]. The equivalent flow stress ($\sigma$) in JC flow stress model is

$$\sigma = [A + B\varepsilon^n][1+cln(\frac{\dot{\varepsilon}}{\dot{\varepsilon}_0})][1 - (T^*)^m] \quad (4)$$

where $A$, $B$, $n$ and $m$ are the constants, $\varepsilon$ is the equivalent plastic strain, $\dot{\varepsilon}$ is the equivalent plastic strain rate, $\dot{\varepsilon}_o$ is the reference equivalent plastic strain rate, $c$ is the non-dimensional strain rate sensitivity and $T^*$ is the normalized temperature expressed as $T^* = (T-T_r)/(T_m - T_r)$; where $T$, $T_r$ and $T_m$ are the temperature, room temperature and melting temperature, respectively. The value of m was taken zero in the simulation. The failure strain ($\varepsilon_f$) in the JC damage model is

$$\varepsilon_f = \left[D_1 + D_2 e^{D_3\sigma^*}\right]\left[1+D_4 ln\left(\frac{\dot{\varepsilon}}{\dot{\varepsilon}_0}\right)\right](1+D_5 T^*) \quad (5)$$

where, $D_1$, $D_2$, $D_3$, $D_4$ and $D_5$ are failure parameters and $\sigma^* = \sigma_m/\sigma$ represents the stress triaxiality ratio, where $\sigma_m$ is the hydrostatic stress. The parameters related with stress triaxiality and temperature were not taken into account ($D_2 = 0$ and $D_5 = 0$) as the stress state and the temperature were assumed to change insignificantly during crushing. The material model parameters were obtained experimentally following the procedures described in the previous section.

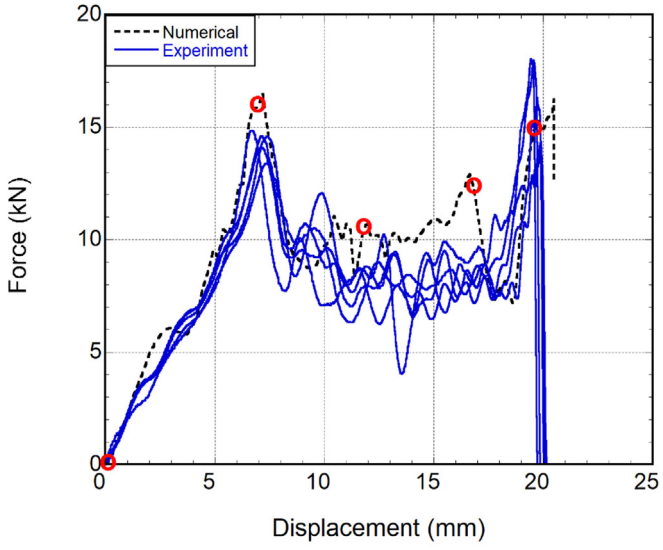


(a)

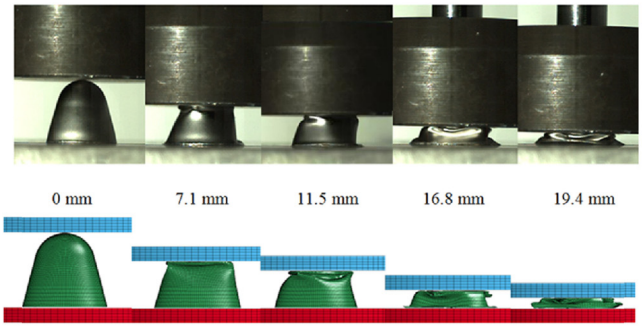


(b)

**Fig. 6.** (a) Experimental (5 tests) and numerical force–displacement curves of the inner core at dynamic strain rates and (b) deformed specimens.

Since the crushing modes of the tested core structure were not axisymmetric, the shells were modelled in full geometry as seen in Fig. 2(b). The model consists of three components: moving top head, specimen and fixed bottom plate. In the model, the rigid bottom plate was fully constrained in all directions, while the rigid top plate was moved only along the loading direction. Numerically trimmed inner core and outer shell or both were imported into the model as specimen. In the quasi-static compression model, a time-dependent displacement curve was defined to the moving top head and mass scaling was applied. In the mass scaling, the deformation rate was increased while the density of the specimen was reduced until the ratio between the kinetic energy and the internal energy was about 5%. In the drop weight numerical model, an initial velocity was defined to the moving top head and the drop weight mass in the experiments was considered as the total weight of the top head. In the dynamic test simulations, the single surface contact algorithm was used in the fold formation and the failure within the specimens. The contact between the specimen and the plates was defined by the surface to surface contact algorithm. The static and dynamic friction coefficients between the specimen and the plates were taken 0.3 and 0.2, respectively. The optimum number of elements for both of the numerical models was determined by conducting a mesh sensitivity analysis. The analysis showed that an element size of 0.5 mm converged to the solutions within a reasonable time. After the numerical studies were verified, both the effects of inertia and strain rate sensitivity of blank material on the deformation behavior of the structure were investigated in detail.

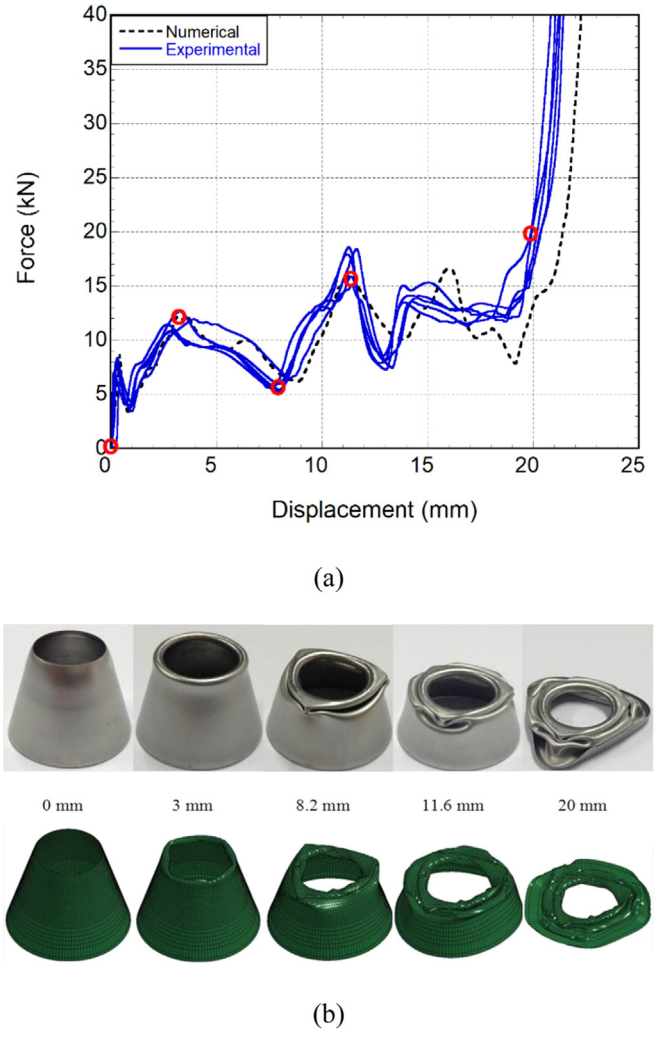


**Fig. 7.** (a) Experimental (5 tests) and numerical force–displacement curves of the outer shell at quasi-static strain rates and (b) deformed specimens.

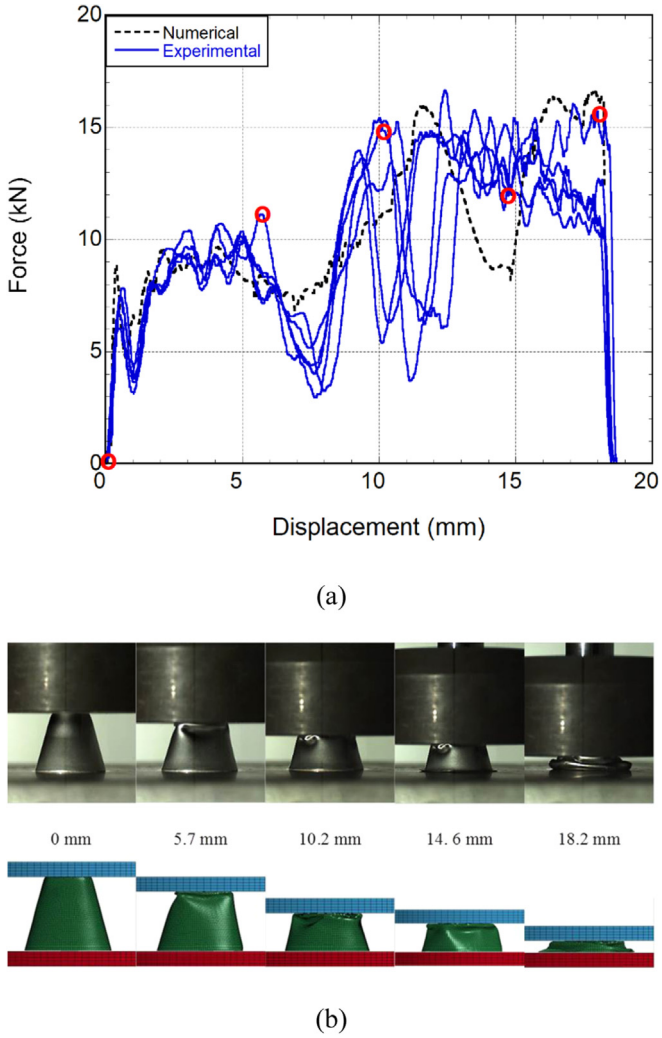


**Fig. 8.** (a) Experimental (5 tests) and numerical force–displacement curves of the outer shell at dynamic strain rates and (b) deformed specimens.

## 4. Results and discussion

The determined JC flow stress and JC failure strain model parameters of AISI 304L stainless steel are tabulated in Table 1. In this table ρ, *G*, *E* and $\nu$ refer to density, shear and elastic modulus and Poisson's ratio, respectively. True stress-true plastic strain curves of AISI 304L stainless steel are shown in Fig. 3(a) at both quasi-static and high strain rates and together with JC flow stress fit using the parameters in Table 1. As seen from the figure, the stainless steel material shows a strain rate dependent yield and flow stress behavior. The yield stress increases from 218 MPa at 0.0007 $s^{-1}$ to 550 MPa at 1580 $s^{-1}$. With the same strain rate range (two different quasi-static strain rate and another high strain rate level), the failure strain decreases from 0.8 to 0.7 as shown in Fig. 3(b). The fitted JC failure strain model parameters are also shown in the same figure.

The measured and numerically determined nonlinear thickness distribution throughout the length of the structure are shown in Fig. 4 for the inner core and outer shell. The top of the specimen was taken as a reference (0 mm) to count the distance of the points. As seen in the same figure, the numerical thickness distributions show well agreements with measured thickness distributions. The thickness at the bottom of the inner core is 0.49 mm, while the thickness reduces to 0.35 mm at the end of the hemispherical cap of the core structure. Similarly, the thickness at the top of the frusto-conical shell is 0.25 mm, the thickness is 0.5 mm at the bottom of this geometry.

Fig. 5(a) shows the typical experimental and numerical quasi-static force-displacement curve of the inner core. The experimental and numerical deformation pictures in Fig. 5(b) correspond to the displacements marked with o in Fig. 5(a). The force values and the deformation modes of the experiment and model seen in Fig. 5(a) and (b) are very similar to each other. The initial near–linear increase of the force values (0–5 mm) in Fig. 5(a) corresponds to the flattening and inward dimpling of the hemispherical cap. This is followed by an asymmetric fold formation. The asymmetric fold formation is completed at about 15 mm displacement. The following peak loads corresponds to the initiation and end of the successive folding. Both experimentally and numerically two folds are formed close to the top section of the specimen. This mode of folding is well accord with the critical ratio, $R/t < 50$, for the asymmetric folding proposed by Gupta et al. [10]. Following the asymmetric fold, the structure is globally compressed, leading to abrupt rise of the force values. For the last stages of the deformation the lower end of the specimen reverse bends and the final folding is reverted to the diamond mode. Fig. 6(a) and (b) show the typical experimental and numerical force-displacement curves and the deformed pictures of the inner core at a dynamic strain rate. The plastic deformation at higher strain rate test also initiates with the flattening of the cap and following axisymmetric folding (Fig. 6(b)). Although, the first fold formation is nearly axisymmetric, the following second folding switches to the diamond mode. Since the diamond mode is a lower mode and it causes a load-drop after the initial peak force. However, the initial peak force of

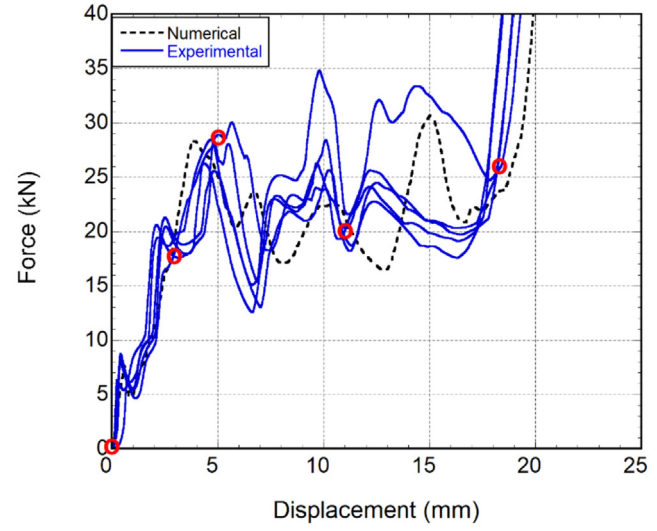


(a)

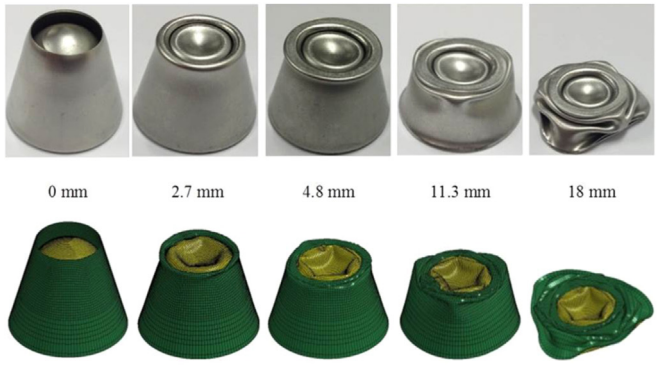


(b)

**Fig. 9.** (a) Experimental (5 tests) and numerical force–displacement curves of the balanus structure at quasi-static strain rates and (b) deformed specimens.

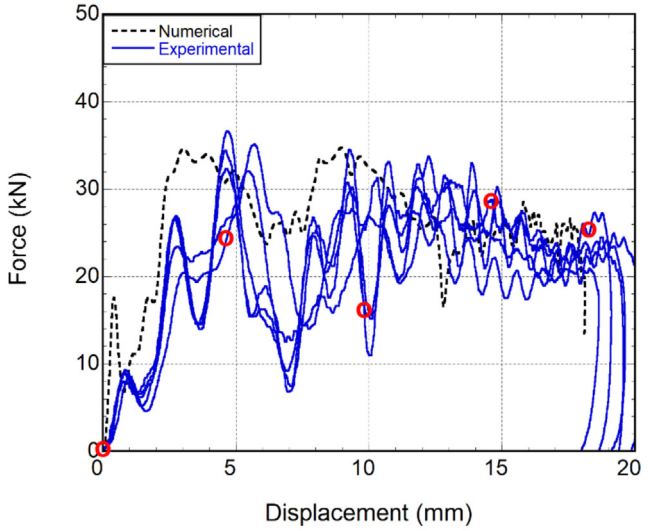


(a)

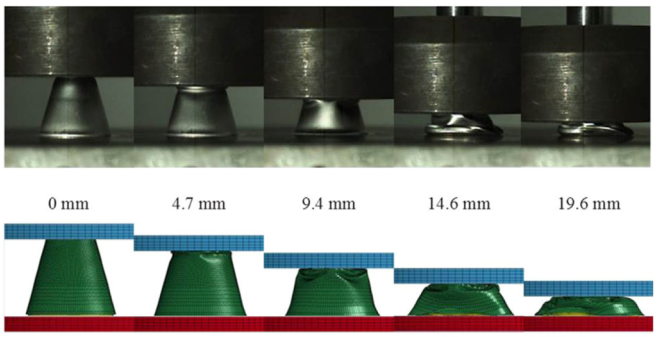


(b)

**Fig. 10.** (a) Experimental (5 tests) and numerical force–displacement curves of the balanus structure at dynamic strain rates and (b) deformed specimens.

dynamically tested specimen is higher than that of quasi-statically tested specimen. As with quasi-static test, the dynamically tested specimens deform in diamond mode at the final stages of the deformation.

The typical experimental and numerical quasi-static force-deformation curves and deformation modes of outer shell shown sequentially in Fig. 7(a) and (b) also display well agreements between each other. Both experimentally and numerically, the initial deformation is the bending of the upper edge which is reflected as an initial load-drop in Fig. 7(a) at 1 mm displacement. Then, the first asymmetric fold starts to form at 3 mm displacement and completed at about 13 mm. Later, the structure is globally bent to give abrupt rise in the force values at 20 mm displacement. The typical dynamic experimental and numerical force-displacement of the outer core is shown in Fig. 8(a). The experimental and numerical dynamic force values show an increase after about 10 mm displacement, while the dynamic deformation mode is very much similar to that of the quasi-static strain rate as seen in Fig. 8(b).

Fig. 9(a) and (b) show sequentially the typical experimental and numerical quasi-static force-displacement curve and the deformation pictures of the balanus structure. At the beginning of the deformation, both balanus structure and outer shell geometries present a significant amount of similarities in the general characteristics of the force displacement curves (the number of peaks and valleys) and the corresponding number of folds. The outer shell and the inner core interact with each other and deform together as the deformation continues. The overall crushing character of the structure is around an average force value. As seen in Fig. 9(a), numerical results of both force-deformation curves and deformation modes are close to the test data. Fig. 9(b) shows that the upper region of the balanus structure is curled inward due to the outer shell structure and the initial peak was observed at about 1 mm of deformation (Fig. 9(a)). The specimens deform in diamond mode and the densification is seen at 18 mm. During the last fold formation which is before the densification, there is a global bending effect in the structure (Fig. 9(b)). This results in a slight variation at the last region of the curves. The numerical deformation forces and behavior of the balanus structure also closely resembles the experimental deformation at dynamic strain rate (Fig. 10(a) and (b)). The initial peak is seen again at about 1 mm and the hemispherical region of the inner core and the upper region of the outer shell interact during the first fold. The force starts to decrease with further deformation and one of the local minimum points is seen at 7 mm of deformation. The other local maximum and minimum points corresponding to the fold formation are observed with further crushing in the curve. These results show that the outer shell confines the inner core when the conical segment of the specimen starts to deform and crushing behavior of the balanus structure resemble the outer shell at the rest of the deformation. Thus, the outer shell improves the load carrying capacity of the balanus structure by means of the confinement effect.

Quasi-static and dynamic experimental results are summarized in

**Table 2**
Quasi-static experimental results of the specimens.

| | $P_i$ (kN) | $P_{mean}$ (kN) | $P_{max}$ (kN) | Energy (J) | Disp. (mm) | SAE (kJ kg$^{-1}$) | SAE at 18.2 mm (kJ kg$^{-1}$) |
|---|---|---|---|---|---|---|---|
| **Core** | 13.2 ± 0.8 | 9.3 ± 0.9 | 13.3 ± 0.7 | 165.2 ± 9.6 | 18.9 | 25.4 ± 1.5 | 24.2 ± 1.3 |
| **Shell** | 7.5 ± 1.0 | 10.5 ± 0.1 | 17.1 ± 1.6 | 198.7 ± 1.9 | 18.9 | 29.3 ± 0.3 | 28.0 ± 0.3 |
| **Balanus** | 7.5 ± 1.2 | 20.8 ± 1.9 | 29.0 ± 3.7 | 385.9 ± 35.4 | 18.5 | 29.1 ± 2.7 | 28.4 ± 2.7 |

**Table 3**
Experimental results of the specimens at dynamic strain rates.

| | $P_i$ (kN) | $P_{mean}$ (kN) | $P_{max}$ (kN) | Energy (J) | Disp. (mm) | SAE (kJ kg$^{-1}$) | SAE at 18.2 mm (kJ kg$^{-1}$) | Test |
|---|---|---|---|---|---|---|---|---|
| **Core** | 14.3 ± 0.6 | 7.9 ± 0.1 | 14.3 ± 0.6 | 149.4 ± 0.9 | 18.9 | 23.0 ± 0.1 | 22.0 ± 0.3 | 4 m s$^{-1}$ 26.63 kg |
| **Shell** | 7.1 ± 0.7 | 9.8 ± 0.3 | 15.2 ± 0.9 | 181.8 ± 6.1 | 18.5 | 26.9 ± 0.9 | 26.6 ± 0.7 | 4 m s$^{-1}$ 28.38 kg |
| **Balanus** | 8.8 ± 0.5 | 21.0 ± 0.8 | 34.1 ± 1.9 | 388.2 ± 14.8 | 18.5 | 29.3 ± 1.1 | 28.8 ± 1.1 | 4 m s$^{-1}$ 59.38 kg |

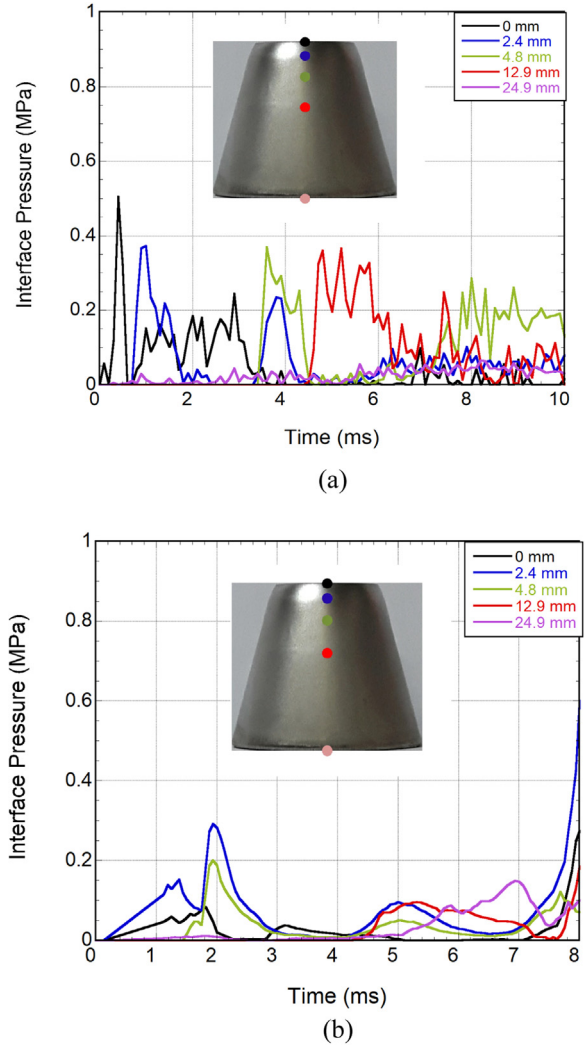


**Fig. 11.** Interface pressure (a) quasi- static and (b) dynamic.

Tables 2, 3. In these tables $P_i$, $P_{mean}$, $P_{max}$ and SAE refer to initial peak force, mean force, maximum force and specific absorbed energy, respectively. The maximum force value in drop weight experiments (33.8 kN) is approximately 16.5% superior than that of the quasi-static (29 kN). The shell absorbs higher energy than the inner core, while the balanus structure absorbs the highest energy at both quasi-static and

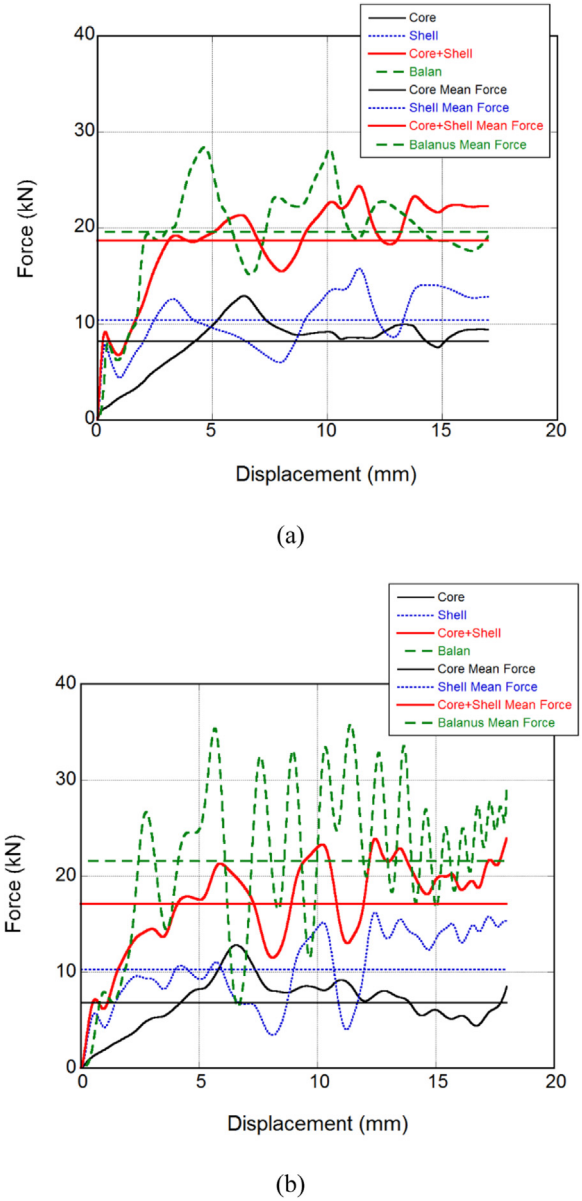


**Fig. 12.** Interaction effect at different strain rate (a) quasi- static and (b) dynamic.

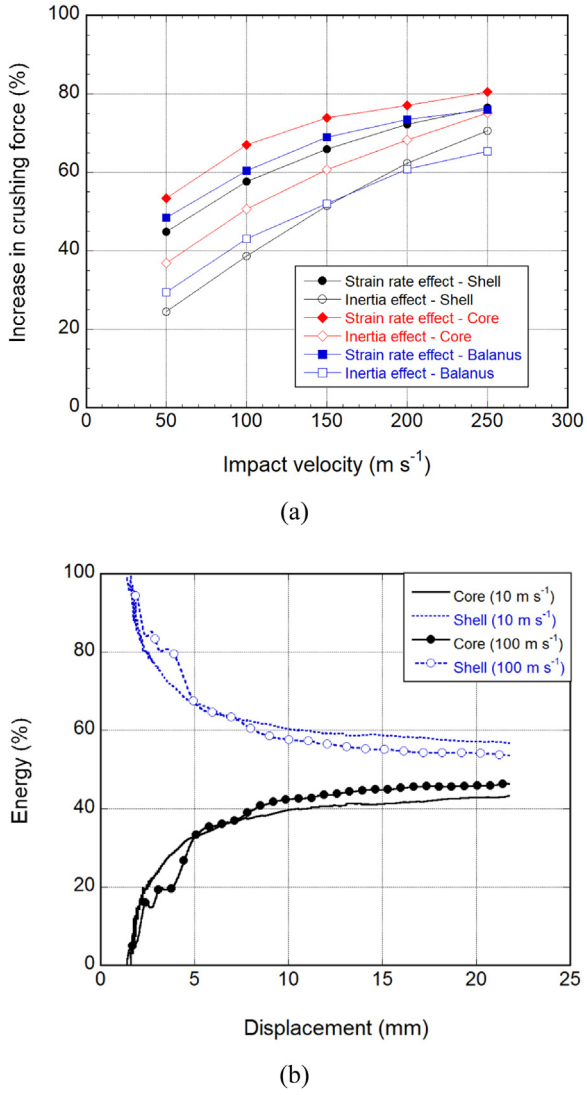


**Fig. 13.** (a) Percentage increase in crush load vs. impact velocity and (b) energy partition.

dynamic strain rates. It is also noted in the same tables that the outer shell and the balanus structure are more efficient in SAE than the inner core at the quasi-static strain rate. However, the balanus structure is the most efficient configuration in terms of energy absorption among all structures investigated in this study at dynamic strain rate. When the strain rate increases, the SAEs of inner core and shell decreases slightly, while the energy absorption characteristic of the balanus structure increases, showing the effect of interaction between core and shell

The increased load carrying capacity of the balanus at quasi-static and dynamic strain rates is ascribed to the interaction between the core and shell and the confinement effect of the outer shell during the crushing. In order to compare the level of interaction between the constituents of the structure at both static and dynamic rates, the interface pressure history between them was plotted for different points in Fig. 11. During the course of deformation outer shell and inner core contact each other and due to this contact an interface pressure is generated. As can be seen from the figure the interface pressure values at dynamic rates exceed those of static showing that the deformation is dominated more due to the interaction effect.

This result is also very well consistent with the previously reported increased force values in bi-tubular structures due to the interaction between tubes [21]. As shown in Fig. 12(a), the mean force of the balanus structure is higher than the mean force of the arithmetic sum of the inner core and shell at quasi-static strain rate. The increase in the mean force at quasi-static strain rate is 5.4%, while this difference reaches to 25.7% at dynamic strain rate as seen in Fig. 12(b). The amount of the increase in load-carrying performance is a clue to understand the intensity of the interaction [11]. Energy absorbing structures are classified as Type I and Type II [32–34]. Type I structures exhibit flat-topped force-displacement curve and inertia insensitive behavior. Type II structures however exhibits a force-drop after the initial peak force and an inertia sensitive behavior. In order to differentia the strain rate effect from the inertial effect, the numerical crushing tests of the core, shell and balanus structure were simulated and the mean force values were determined at five different impact velocities; 50, 100, 150, 200 and 250 $m\,s^{-1}$, with and without considering strain rate sensitivity. The increases in the force due to strain rate and inertia are shown in Fig. 13(a). As seen in the same figure, the increase in crush force due to strain rate and inertia increases as the velocity increases. While, the strain rate has higher contribution on the increase in the crush force for each geometry investigated. It is concluded that the bio-inspired structure and its components show Type II behavior. The percentages of the energy absorption energy-displacement curves of core and shell at 10 and 100 $m\,s^{-1}$ are shown in Fig. 13(b). The outer shell absorbs higher energy than the inner core at the beginning of the deformation. However, the difference between the energy absorption partitions of the shell and core decreases as the deformation increases. At the end of the deformation, the outer shell absorbs 56.7% of the total energy, whereas the inner core absorbs 43.3% of the total energy at 10 $m\,s^{-1}$. As the impact velocity increases to 100 $m\,s^{-1}$, the difference between the energy absorption capacities of the core and shell decreases. At the end of the deformation, the shell absorbs 53.6% and the core absorbs 46.4% of total energy.

## 5. Conclusions

The crushing behavior and energy absorbing performance of a bio-inspired geometry consisting of an inner core and an outer shell, called balanus structure, were investigated at different strain rates both experimentally and numerically. The structure was formed by deep drawing process and the deep drawing process was also modelled using nonlinear finite element code LS-DYNA to determine the residual stress/strain and the non-linear thickness distribution after the forming process. The compression test models performed on the inner core, the other shell and the balanus structure at quasi-static and dynamic strain rates showed well agreements with the experiments. The deformation modes of the inner core, outer shell and balanus structure did not change significantly with the strain rate and the structures deformed in diamond mode following an initial concertina mode. The force-deformation curve of the balanus structure was found to be above the arithmetic sum of the force-deformation curves of the inner core and the outer shell. The increase in mean crushing force of the balanus structure was 5% at quasi-static strain rate, but increased to roughly 26% at dynamic strain rate. The increased load carrying capacity of the balanus at quasi-static and dynamic strain rates was ascribed to the interaction between the core and shell and the confinement effect of the outer shell particularly at dynamic strain rate. According to the results acquired from numerical models, the outer shell absorbed more energy than the inner core throughout the deformation history. Nevertheless, the difference of the energy absorbing performance between the constituents of the balanus structure decreased with the increase in the deformation rate. The effect of strain rate and inertia on the increase in crushing force increased with increasing impact velocity, while the strain rate effect had greater influence than the inertia on the crushing force.

## Acknowledgements

The authors would like to thank The Scientific and Technological

Research Council of Turkey (TUBITAK) for the Grant #214M339.

## References


[1] J.M. Alexander, An approximate analysis of the collapse of thin cylindrical shells under axial loading, Q. J. Mech. Appl. Math. 13 (1) (1960) 10–15.
[2] T. Wierzbicki, W. Abramowicz, On the crushing mechanics of thin-walled structures, J. Appl. Mech. 50 (4a) (1983) 727–734.
[3] S.R. Reid, T.Y. Reddy, Static and dynamic crushing of tapered sheet-metal tubes of rectangular cross-section, Int. J. Mech. Sci. 28 (9) (1986) 623–637.
[4] L. Mirfendereski, M. Salimi, S. Ziaei-Rad, Parametric study and numerical analysis of empty and foam-filled thin-walled tubes under static and dynamic loadings, Int. J. Mech. Sci. 50 (6) (2008) 1042–1057.
[5] G.M. Nagel, D.P. Thambiratnam, A numerical study on the impact response and energy absorption of tapered thin-walled tubes, Int. J. Mech. Sci. 46 (2) (2004) 201–216.
[6] N.K. Gupta, G.L.E. Prasad, S.K. Gupta, Plastic collapse of metallic conical frusta of large semi-apical angles, Int. J. Crashworthines 2 (4) (1997) 349–366.
[7] N.K. Gupta, N.M. Sheriff, R. Velmurugan, A study on buckling of thin conical frusta under axial loads, Thin Wall Struct. 44 (9) (2006) 986–996.
[8] N.K. Gupta, Venkatesh, Experimental and numerical studies of impact axial compression of thin-walled conical shells, Int. J. Impact Eng. 34 (4) (2007) 708–720.
[9] N.M. Sheriff, N.K. Gupta, R. Velmuruganc, N. Shanmugapriyan, Optimization of thin conical frusta for impact energy absorption, Thin Wall Struct. 46 (6) (2008) 653–666.
[10] N.K. Gupta, N.M. Sheriff, R. Velmurugan, Analysis of collapse behaviour of combined geometry metallic shells under axial impact, Int. J. Impact Eng. 35 (8) (2008) 731–741.
[11] A. Tasdemirci, S. Sahin, A. Kara, K. Turan, Crushing and energy absorption characteristics of combined geometry shells at quasi-static and dynamic strain rates: experimental and numerical study, Thin Wall Struct. 86 (2015) 83–93.
[12] S.R. Reid, T.Y. Reddy, M.D. Gray, Static and dynamic axial crushing of foam-filled sheet-metal tubes, Int. J. Mech. Sci. 28 (5) (1986) (295-&).
[13] W. Abramowicz, T. Wierzbicki, Axial crushing of foam-filled columns, Int. J. Mech. Sci. 30 (3–4) (1988) 263–271.
[14] S.P. Santosa, T. Wierzbicki, A.G. Hanssen, M. Langseth, Experimental and numerical studies of foam-filled sections, Int. J. Impact Eng. 24 (5) (2000) 509–534.
[15] H.R. Zarei, M. Kroger, Optimization of the foam-filled aluminum tubes for crush box application, Thin Wall Struct. 46 (2) (2008) 214–221.
[16] A.K. Toksoy, M. Guden, The strengthening effect of polystyrene foam filling in aluminum thin-walled cylindrical tubes, Thin Wall Struct. 43 (2) (2005) 333–350.
[17] M. Guden, A.K. Toksoy, H. Kavi, Experimental investigation of interaction effects in foam-filled thin-walled aluminum tubes, J. Mater. Sci. 41 (19) (2006) 6417–6424.
[18] S. Santosa, T. Wierzbicki, Crash behavior of box columns filled with aluminum honeycomb or foam, Comput. Struct. 68 (4) (1998) 343–367.
[19] A.A. Nia, M. Parsapour, Comparative analysis of energy absorption capacity of simple and multi-cell thin-walled tubes with triangular, square, hexagonal and octagonal sections, Thin Wall Struct. 74 (2014) 155–165.
[20] M.D. Goel, Deformation, energy absorption and crushing behavior of single-, double- and multi-wall foam filled square and circular tubes, Thin Wall Struct. 90 (2015) 1–11.
[21] M.H. Kashani, H.S. Alavijeh, H. Akbarshahi, M. Shakeri, Bitubular square tubes with different arrangements under quasi-static axial compression loading, Mater. Des. 51 (2013) 1095–1103.
[22] D. Smith, C. Graciano, G. Martinez, Quasi-static axial compression of concentric expanded metal tubes, Thin Wall Struct. 84 (2014) 170–176.
[23] D. Smith, C. Graciano, G. Martinez, P. Teixeira, Axial crushing of flattened expanded metal tubes, Thin Wall Struct. 85 (2014) 42–49.
[24] J.W. Xiang, J.X. Du, Energy absorption characteristics of bio-inspired honeycomb structure under axial impact loading, Mater. Sci. Eng. A-Struct. 696 (2017) 283–289.
[25] H. Rhee, M.F. Horstemeyer, Y. Hwang, H. Lim, H. El Kadiri, W. Trim, A study on the structure and mechanical behavior of the Terrapene carolina carapace: a pathway to design bio-inspired synthetic composites, Mater. Sci. Eng. C-Mater. 29 (8) (2009) 2333–2339.
[26] J.X. Chen, C.L. Gu, S.J. Guo, C.F. Wan, X. Wang, J. Xie, X.Q. Hu, Integrated honeycomb technology motivated by the structure of beetle forewings, Mater. Sci. Eng. C-Mater. 32 (7) (2012) 1813–1817.
[27] X.F. Yang, J.X. Ma, Y.L. Shi, Y.X. Sun, J.L. Yang, Crashworthiness investigation of the bio-inspired bi-directionally corrugated core sandwich panel under quasi-static crushing load, Mater. Des. 135 (2017) 275–290.
[28] ASTM, Standard test methods for tension testing of metallic materials, ASTM E8M-04, West Conshohocken, Pennsylvania, USA, 2004.
[29] LSTC, LS-DYNA: Keyword User's Manual, (2007).
[30] Z. Maker, A procedure for springback analysis using LS-DYNA.
[31] G.R. Johnson, A constitutive model and data for metals subjected to large strains, high strain rates and high temperatures, in: Proceedings of the 7th International Symposium on Ballistics, The Hague, Netherlands, 1983, 1983.
[32] T.G. Zhang, T.X. Yu, A note on a velocity sensitive energy-absorbing structure, Int. J. Impact Eng. 8 (1) (1989) 43–51.
[33] L.L. Tam, C.R. Calladine, Inertia and strain-rate effects in a simple plate-structure under Impact loading, Int. J. Impact Eng. 11 (3) (1991) 349–377.
[34] C.R. Calladine, R.W. English, Strain-rate and inertia effects in the collapse of 2 types of energy-absorbing structure, Int. J. Mech. Sci. 26 (11-1) (1984) (689-&).
[35] ⟨http://www.seanature.co.uk/intertidal_tregardock_beach.html⟩.